PAPER

Enhanced electrochemical performance of morphology-controlled titania-reduced graphene oxide nanostructures fabricated *via* a combined anodization-hydrothermal process†

V. C. Anitha,‡ Nazanin Hamnabard,‡ Arghya Narayan Banerjee,* G. R. Dillip and Sang Woo Joo*

Titania nanotubes (TNTs) synthesized by an anodization process were used as a basic substrate material to create different morphologies of quasi-1D (nanoribbons), 2D (nanoflakes), and 3D (nanoparticles) structures *via* an alkali-controlled hydrothermal route. Graphite oxide was introduced to the hydrothermal unit to fabricate graphene oxide/reduced graphene oxide–titania nanostructure hybrid materials. The presence of NaOH and graphene oxide in the hydrothermal environment had a profound effect on the surface morphology of the nanostructures. NaOH acted as both an etchant to convert TNT surfaces into low-dimensional structures and as a reducing agent to convert graphene oxide into reduced graphene oxide. Graphene oxide inhibited the etching rate to tune the surface morphologies into 1D, 2D, and 3D nanostructures. The electrochemical supercapacitance of all the nanostructures was characterized. Among the prepared samples, the nanostructured hybrid sample of reduced graphene oxide, titania nanoflakes, and TNT exhibited enhanced electrochemical performance with quite high specific capacitance. This superior electrochemical performance is attributed to the specific nanostructure, which provides short pathways for fast transport of salt ions and improved specific surface area for more adsorption sites for the formation of an electrical double layer, which leads to fast charge transfer.

1. Introduction

Among emerging power storage devices, electrochemical capacitors (or supercapacitors) have attracted growing interest for energy storage due to their high power density, good stability, and long cycle life.[1–3] There are two common categories of supercapacitors based on the charge storage mechanism. The first is electrical double-layer capacitors (EDLCs), which contribute a nonfaradaic charge separation at the electrode/electrolyte interface. The other is pseudocapacitors, which are based on faradic processes (redox reactions) at or near the surface of active materials.[4,5]

Titania nanotubes (TNTs) are pseudocapacitance materials that can be prepared by a simple and low-cost anodic oxidation method. They have been explored as current collector materials in supercapacitors because of their chemical stability, non-toxicity, abundance, and special geometry.[6–10] However, their poor electrical conductivity, low cyclability, and the

irreversibility of the faradic reactions on the electrode surface of TiO_2 are obstacles in the development of high-performance supercapacitors.[4,11] Therefore, a combination of electrical double-layer and pseudocapacitors is considered to be the best way to enhance the performance of supercapacitors.[10]

Graphene is a two-dimensional giant molecule of sp^2-bonded carbon atoms and is considered to be one of the most ideal candidates for supercapacitors because of its excellent electrical and optical properties, large specific surface area, and outstanding mechanical properties. The unique properties of this material include a surface area of 2630 m^2 g^{-1}, a charge carrier mobility of 200 000 cm^2 V^{-1} s^{-1}, and a thermal conductivity of 5000 W m^{-1} K^{-1}. Recent research has shown that graphene forms a more efficient conducting network compared to the widely used carbon black and even carbon nanotubes.[12–14] The high surface area, electrical conductivity, and activity of incorporated graphene have led to many advances in nanomaterial-based supercapacitors. Graphene layers can play an important role in improving the adhesion of pseudo-species for enhanced cycling stability. Graphene can also increase charge transport between the electrode and pseudo-species and the specific loading of pseudo-species for higher energy.[15]

Although graphene is a great conductor, it is not very good at collecting and storing charge because the electrons in graphene

School of Mechanical Engineering, Yeungnam University, Gyeongsan 712-749, South Korea. E-mail: banerjee_arghya@hotmail.com; arghya@ynu.ac.kr; swjoo@yu.ac.kr; Fax: +82-53-810-2062; +82-53-810-2062; Tel: +82-53-810-2453; +82-53-810-3239

† Electronic supplementary information (ESI) available. See DOI: 10.1039/c5ra23722j

‡ Authors contributed equally.

can penetrate any potential barrier, thus making the device "leaky," even in open-circuit conditions. Hence, researchers have focused on finding appropriate ways to modify graphene to reduce its conductivity to an appropriate level that is suitable for charge storage and similar electronic applications. Hydrogenated carbon ("graphane"[16]) and graphene oxide (GO)[17] are suitable candidates for supercapacitor applications. Graphene oxide contains a range of reactive oxygen functional groups, such as carboxyl, hydroxyl, epoxy, and keto groups, through which its electrical characteristics can be tuned *via* chemical functionalization. A variety of thermal and mechanical methods can be used to exfoliate graphite oxide to GO, but sonicating and/or stirring graphite oxide in water are the most commonly used.[17]

GO is chemically similar to graphite oxide but structurally different. The graphite oxide is exfoliated into monolayers or few-layered stacks (GO structure) rather than a stacked structure. Hence, GO cannot be used as a conductive material for electrical and electrochemical devices, and it is essential for GO to be reduced to ensure electronic conjugation.[5] Chemical or high-temperature treatment of GO is required to convert it to the electrically conductive reduced GO (RGO).[18] RGO obtained by chemical, thermal, or electrochemical methods can show improved electrical and electrochemical properties compared to pure GO due to a large surface area, high electrical conductivity, and porous macrostructure.

One of the main strategies for fabricating TiO_2 nanomaterial-based electrodes is the construction of a three-dimensional (3D) nanostructured network to provide a large electrode–electrolyte contact area for higher charge transfer. Another is the incorporation of conductive materials like reduced GO in a titania matrix[18] to accelerate the charge transfer process. Based on these strategies, we have designed a TiO_2/graphene nanocomposite-based electrode by incorporating RGO into titania nanostructures like TiO_2 nanoflakes, nanotubes, and nanoparticles. Various reports have focused on the construction and systematic investigation of graphene–titania hybrids/nanocomposites for supercapacitor electrodes.[19,20] Notably, in the most common methods, commercially available Degussa P25 nanoparticles and titanium alkoxides have widely been employed as a titania precursor and used as a counterpart to graphene in composites. To the best of our knowledge, there has been no report on the formation of reduced graphene–titania hybrid nanostructures using a 3D network of anodized titania nanotube arrays as a support for electrochemical capacitor applications.

We fabricated a composite nanostructure comprising RGO, titania nanoflakes, and TNTs (denoted as TRGNF), as well as one consisting of GO, titania nanoparticles, and TNTs (denoted as TGNP). This was achieved using a facile and green combined anodization-hydrothermal approach. These composites were then used in electrochemical capacitors. Oxidative formation of TNTs was first done by applying an anodizing electric field between Ti foil and Pt electrodes, followed by hydrothermal syntheses of GO/RGO onto a TNT surface. The novelty of the fabrication process is that the presence of an alkali medium during hydrothermal treatment simultaneously reduces the GO into RGO and etches the TNT surface into 2D nanoflake structures. The absence of the medium creates TiO_2 nanoparticulate structures with GO deposited on them. The alkaline solution (NaOH) was strong enough to reduce the GO without any toxic reducing agents like $NaBH_4$.[11]

The physicochemical properties of the composites were then examined with a combination of physical and electrochemical characterization techniques. TRGNF showed enhanced electrochemical performance compared to the other samples because of the superior physico-chemical properties based on the synergetic effect of RGO and titania nanoflakes. The results could open up new avenues for developing a novel reduced graphene–titania hybrid for supercapacitor applications.

2. Experimental methods

2.1. Materials

Graphite powder was purchased from Kanto Chemical Co. Inc., Japan. Ti foil (99.7% purity, 0.1 mm thickness), potassium permanganate ($KMnO_4$, 99%), sodium hydroxide (NaOH, 98% purity), and potassium chloride (KCl, 99% purity) were obtained from Sigma Aldrich. Sulfuric acid (H_2SO_4, 95% purity), hydrogen peroxide (H_2O_2, 30% purity), nitric acid (HNO_3, 61% purity), hydrofluoric acid (HF, 50% purity), hydrochloric acid (HCl, 37% purity) and acetone (99.5% purity) were purchased from Duskan Pure Chemicals Co. Ltd., Korea. All chemicals were of the highest purity available and used without further purification.

2.2. Preparation of samples

2.2.1. Synthesis of titania nanotubes. Titanium foils (14 mm^2 area) were ultrasonically cleaned in acetone and deionized water sequentially and then air-dried at room temperature. Short, robust, and highly ordered titania nanotube arrays were fabricated by the anodic oxidation of metallic Ti foil in 0.5 wt% hydrofluoric acid (HF) solution. In detail, Ti foil was immersed in 30 ml of the fresh electrolyte. Then, a two-electrode system consisting of Ti foil was used as an anode with a platinum plate as the cathode and subjected to potentiostatic anodization at 20 V for 20 minutes.[11,21] Finally, the anode was taken out of the electrolyte, thoroughly rinsed with DI water, and air dried at room temperature. The details of the anodization process are reported elsewhere.[22,23]

2.2.2. Synthesis of graphene oxide. GO formation is a two-step process. Firstly, graphite oxide was prepared by adding graphite powder to mixture of concentrated acids including $H_2SO_4 : H_3PO_4$ (160 : 40 ml) with constant stirring.[24] Then, 9 g of potassium permanganate ($KMnO_4$) was slowly added to the mixture with continuous stirring at room temperature. After 5 days of ageing, 6 ml of 30% aqueous hydrogen peroxide (H_2O_2) was added drop by drop to quench the solution. Bubbles were observed in the aqueous mixture along with a color change to a bright yellow gel, indicating a higher oxidation state of graphite. The as-formed yellow sediment was centrifuged and washed with an aqueous solution of 1 M HCl to remove insoluble ionic impurities, followed by repeated rinsing with DI water to adjust the natural pH by removing the acid. Finally, the

product was left to dry in the vacuum oven (DZF-6030A) at 333 K for 24 h. In the second step, this graphite oxide (0.1 g) was dispersed in 20 ml of de-ionized water and sonicated for 1 h in a water bath to make a dark brown, stable, and homogeneous GO solution.

2.2.3. Synthesis of titania–reduced GO hybrid nanostructure. The titania–RGO (TRGNF) composite nanostructure was obtained by a facile assembly method.[25] The titania nanotubes fabricated on a Ti foil substrate were placed at the bottom of a 50 ml Teflon-lined stainless-steel capsule. A mixture of aqueous NaOH (10 ml, 2.5 molar) and 20 ml of GO solution was added to the Teflon-lined stainless-steel container. The system was sealed and kept in a furnace (Lindberg/Blue M, Thermo Scientific, Box Furnace) at 150 °C for 24 h and then cooled to room temperature naturally. This resulted in the formation of titania–reduced GO nanoflakes. The final product was removed and rinsed with HCl (0.1 M) and water several times and dried at room temperature.

For comparison of the electrochemical performance, two other structural variants of the sample were fabricated: titania nanoparticle–GO (TGNP) nanocomposites and titania nanoribbons (TNR). These two samples were synthesized by the similar procedure under hydrothermal conditions of 150 °C, 24 h. In particular, TGNP samples were prepared by using titania nanotubes (on Ti foil substrate) and 0.1 g of GO dispersed in 20 ml of de-ionized water without any addition of NaOH. Whereas, TNR samples were prepared by using titania nanotubes (on Ti foil substrate) with 20 ml of 2.5 M NaOH without any addition of GO. Therefore, TGNP samples were prepared by using only GO (and without using any NaOH), whereas TNR samples were prepared by using only NaOH (and without using any GO). Fig. 1 shows a schematic diagram for the syntheses of the samples. RGO was also fabricated separately using a hydrothermal process in the presence of NaOH in the same conditions.

Fig. S1† shows the XRD pattern (S1a), SEM image (S1b) and Raman spectrum (S1c) of the RGO. The two main characteristic peaks D (1352 cm^{-1}) and G (1593 cm^{-1}) for RGO is evident in Fig. S1c† (details are given in Section 3.4).[26,27] Each experiment was repeated three times with a new pair of samples as the working electrode. The three experiments indicate very good reproducibility of the electrodes.

2.3. Characterization

The crystalline structures of the prepared samples were identified at room temperature using X-ray diffraction (XRD) on a diffractometer (D8 Advance, Bruker Germany) with monochromatic high-intensity Cu K$_\alpha$ radiation ($\lambda = 1.5406$ Å), an accelerating voltage of 40 kV, and cathode current of 30 mA. The surface morphology of the samples was characterized *via* scanning electron microscope (SEM) using an S-4200 instrument (Hitachi, Japan). The morphological dimensions are confirmed by using a high resolution transmission electron microscope (HR-TEM) (G^2 F20, Tecnai, Japan). For HR-TEM analysis, the nanotubes/composite nanostructures are lifted off from the metallic Ti substrate and dispersed in alcohol, and drop-casted onto a carbon-coated Cu grid. X-ray photoelectron spectroscopy (XPS) measurements were performed using a spectrometer (K-ALPHA, Thermo Scientific, U.K.) with a pass energy of 30.00 eV. The XPS results were collected in binding energy form and fitted using a mixture of Gaussian (70%) and Lorentzian (30%) GL3 functions (Avantage Software). All the binding energies (BEs) obtained in the XPS analysis are calibrated using the C 1s peak at binding energy 284.5 eV as the reference. Raman spectroscopy measurements were carried out using Raman spectroscopy with laser excitation of 532 nm (HORIBA Scientific, Xplora plus-France). The absorption spectra were analyzed with a UV-vis spectrophotometer (Varian Cary 3 Bio, Australia).

2.4. Electrochemical measurements

Electrochemical experiments were carried out on a CHI660C electrochemical workstation (CH Instruments Inc., USA) using a three-electrode configuration at room temperature. An electrolyte solution of 1 M KCl, Ag/AgCl (agar-saturated KCl), a reference electrode, and a platinum wire used as the counter electrode. Cyclic voltammetry (CV) was performed over a voltage range of −0.2 to 0.7 V at various scan rates (10 to 500 mV s^{-1}). Chronopotentiometry or charge–discharge methods were used to determine the capacitance by varying the current densities (1–10 µA cm^{-2}). Electrochemical impedance spectroscopy (EIS) measurement was performed between 50 kHz and 0.001 Hz using a 5 mV rms sinusoidal modulation at a bias potential of −0.2 V. The specific capacitance was calculated by integrating the area under the CV curves based on the following equation:[18]

$$C = \frac{1}{A\nu(V_2 - V_1)} \int_{V_1}^{V_2} I(V)dV \qquad (1)$$

where ν (V s^{-1}) is the scan rate, $(V_2 - V_1)$ is the potential window, and A (cm^2) is the area of the working electrode. The specific
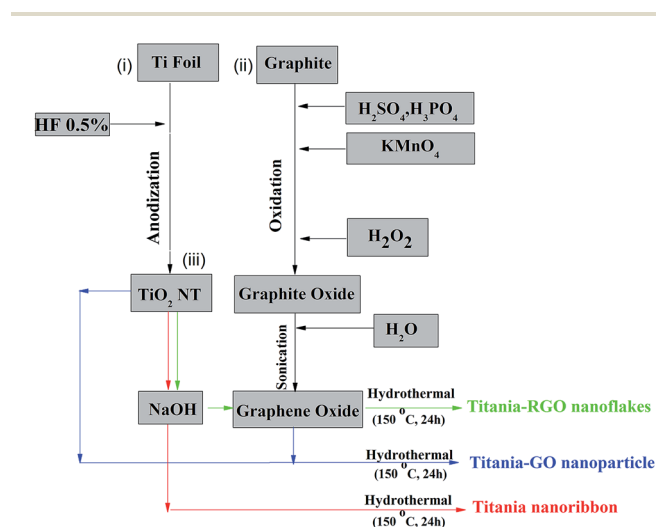

Fig. 1 Schematic diagram of synthesis procedure using TNTs as base materials by a hydrothermal process for (i) titania nanotubes (TNTs) by anodization, (ii) graphene oxide by wet-chemical route, (iii) composite nanostructures containing titania nanoribbon, nanoparticle/GO, nanoflakes/RGO.

capacitance can be calculated from the galvanostatic charge–discharge curve according to the following equation:[18]

$$C = \frac{I\Delta t}{\Delta VA} \qquad (2)$$

where C (F cm^{-2}) is the specific capacitance, I (A) is the discharge current, Δt (s) is the discharge time, ΔV (v) is the potential change during discharge, and A (cm^2) is the area of electrode.

3. Results and discussion

3.1. SEM and TEM studies of different nanostructures

Fig. 2a–d show the FE-SEM images of the as-prepared bare TNTs, TNR, TGNP, and TRGNF composite nanostructures, respectively. Some of the lateral views are shown in the corresponding insets. As shown in Fig. 2a, anodized TNTs had a 1D structure with average inner pore diameter of 80 ± 6 nm, wall thickness of 20 ± 5 nm, and tubular length of 400 ± 50 nm. After the hydrothermal process, a gradual change of the surface morphology on the top surface of the TNTs was observed, as shown in Fig. 2b–d. The titania nanoribbons (TNR, Fig. 2b) are interconnected with each other to form a continuous 3D nanostructure in which individual ribbons have a very high aspect ratio. The nanoribbons have an average 5 ± 2 nm width and 300 ± 50 nm lengths.

The TGNP composite nanostructures are shown in Fig. 2c. The SEM image reveals the typical appearance of non-homogenous agglomerated nanoparticulate structures with some voids in between, with the top surface being covered with GO. The functional groups present in the GO can anchor titania nanoparticle of TGNP *via* hydrogen bond and van der Waals interactions. Fig. 2d shows the TRGNF image, which indicates that the 3D composite structure consists of embedded titania nanoflakes within an RGO layer. The dense and compact film consists of many horizontal individual flakes on the surface of

TNTs, which could improve the surface area of the TRGNF. NaOH acts as a reducing agent on the GO during the hydrothermal process.[28] Additionally, the presence of GO inhibits the etching of TNTs *via* NaOH and helps to transform the TNT surface into 2D nanoflakes rather than 1D nanoribbon structures.

TEM images of titania nanotubes, TNR, TGNP and TRGNF sample are shown in Fig. S2.† Fig. S2(a)† shows the cross-sectional TEM micrograph of nanotubes and corresponding top-view is shown in the inset. The inner pore diameter and wall thickness are consistent with those measured from SEM images. Fig. S2(b)† represents the TEM image of the 1D TNR sample and corresponding HR-TEM image of a single nanoribbon is shown in the inset. Proper lattice spacing of the anatase titania is also indicated in the image. Fig. S2(c) and (d)† represent the HRTEM images of TGNP and TRGNF samples, respectively. The formation of GO/RGO on titania is clearly shown by the proper lattice spacings of the corresponding materials.[29] The insets of Fig. S2(c) and (d)† represent the corresponding low magnification TEM images of TGNP and TRGNF samples.

3.2. XRD analysis

XRD technique was used to analyze the crystal structure of TNT, TNR, TGNP, and TRGNF. The XRD spectra of all the samples are shown in Fig. 3. All the diffraction peaks are attributed to titania with brookite, anatase, and rutile phases and the Ti substrate. In all the samples, the peak at 34.3° corresponds to the diffraction of the (002)/(103) crystal planes of the brookite/anatase phase. The peaks around 62.2° and 75.5° are assigned to the diffraction peaks of the (213) and (215) crystal planes of anatase titania, respectively. The peak around 76.6° is attributed to the diffraction of the (202) crystal plane of rutile titania (JCPDS 29-1360, 21-1276, 21-1272).

No obvious peak was observed for GO/RGO in the TGNP and TRGNF samples. This is because of the lesser percentage of crystalline phase of the carbon material, which leads to very weak XRD signal for the graphitic carbon, and hence, cannot be
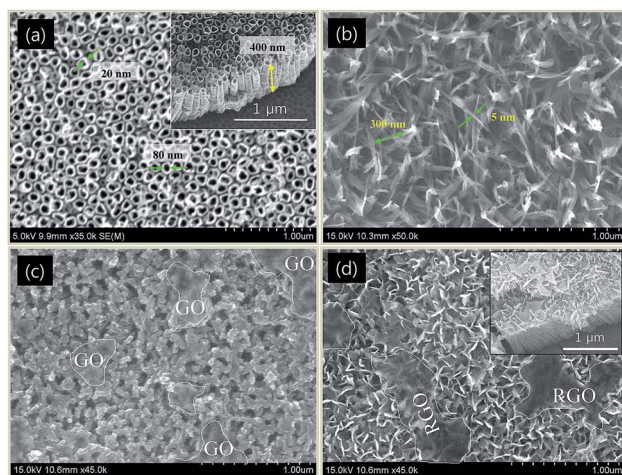

Fig. 2 FE-SEM images of (a) titania nanotubes (TNTs), (b) titania nanoribbons (TNR), (c) titania nanoparticle–GO composite (TGNP), (d) titania nanoflake–RGO composite (TRGNF). Insets of (a) and (d) show the corresponding lateral views.
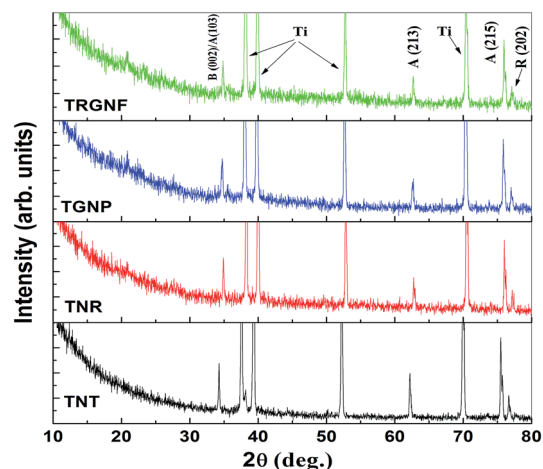

Fig. 3 XRD patterns of TNT, TNR, TGNP, and TRGNF samples.

distinguished from the background noise. It is to be noted in this connection that, the XPS data (shown later) depict the presence of considerable amount of carbon in TGNP and TRGNF. This is because the XPS measurement provides the information of both amorphous and crystalline phases of materials as a whole. In the present study, due to the higher percentage of amorphous phase of the carbon, comparatively higher signal for C is observed in XPS data. However, the presence of GO/RGO in TGNP/TRGNF electrode samples is indicated by the SEM images (Fig. 2c and d) and Raman analysis (Fig. 5, shown later). Also the presence of RGO in TRGNF was qualitatively verified by UV-Vis absorption measurements (Fig. S3†). The bandgap calculations showed a red-shift of the bandgap for TRGNF over TNT (control sample), indicating chemical interaction between TNT and RGO during the hydrothermal process and confirms the presence of RGO in TRGNF sample (this may have resulted from the formation of Ti–O–C chemical bonds, which were confirmed by the XPS data in Section 3.3.3.).

The shift of the main peaks in the XRD data at about 7° for TNR and 1–2° for the TGNP and TRGNF samples can be observed, in contrast to the TNT control sample. The 2θ variations could be due to the higher strain induced during the formation of nanoribbons (TNR), nanoparticles (TGNP), and nanoflakes (TRGNF) by the hydrothermal process.[30] Also, peak broadening is observed for TGNP and TRGNF films in comparison with TNT and TNR, which is due to the incorporation of GO/RGO layers on bare TNTs.[31] The presence of identical crystal planes for all the samples indicates that the hydrothermal treatment basically induces a morphological change in the samples without changing their chemical nature.

3.3. XPS studies

XPS technique was used to analyze the chemical composition and bonding information of synthesized nanostructures. This confirms the C, O, and Ti composition in all the nanostructured samples (Fig. S4†). The Ti signal is less detectable compared to those of C and O in the TRGNF survey spectrum in Fig. S4d.† This indicates that the titania is mostly wrapped in RGO layers. Surface scans of the samples were used to distinguish the elements on the surface.

The peak positions (binding energies) of different elemental core-level spectra and their origins are given in Table 1, and the corresponding elemental compositions are given in Table 2. A high value of C is observed for pure TiO$_2$ (TNT) due to

Table 2 XPS analyses results of the synthesized samples and atomic weight percent and C/O and O/Ti ratios

Sample	Elemental percentage [at%]					Elemental ratio	
	Ti	O$_{(Ti)}$	O$_{(C,OH)}$	O$_{vacancy}$	C	O$_{(Ti)}$/(Ti)	C/O$_{(C)}$
TNT	3.10	3.94	17.97	—	74.99	1.3	—
TNR	25.44	38.79	18.97	8.43	8.37	1.5	—
TGNP	8.24	14.70	23.55	—	53.5	1.8	2.3
TRGNF	7.70	14.66	5.08	—	72.56	1.9	14.2

adsorption of CO$_2$ and other organic substances from the ambient atmosphere.[32] This large amount of C resulting from the experimental conditions or atmospheric contamination is not uncommon. Haddow *et al.*[33] observed nearly 50% carbon in air-annealed titania samples. In the present case, the carbon content was higher since the TNT samples were not annealed. When these TNT samples are hydrothermally treated, some of the atmospheric carbon is oxidized into a gaseous phase. Hence, the C content is decreased in the TNR samples.

In the TGNP and TRGNF samples, the addition of GO again increases the C content, as depicted in Table 2. In addition to O 1s and C 1s peaks, Ti 2p and Ti 3p–3s peaks were also observed in the XPS survey spectra (Fig. S4†). Although Ti 2p is the main Ti peak in the TiO$_2$ structure, the presence of Ti 3p–3s is not uncommon even in single crystalline TiO$_2$, as the bonding between Ti and O is not fully ionic. Hence, the ground state comprises a mixture of Ti^{4+}, Ti^{3+}, and Ti^{2+} with the 3d electrons of Ti^{4+} and Ti^{3+} being transferred from the 2p levels of oxygen.[34]

3.3.1. Analysis of Ti 2p spectrum. The Ti 2p spectrum was obtained from Ti curves, which correspond to the Ti^{4+} state (Fig. 4a). The double peak of spin–orbit components (2p$_{3/2}$ and 2p$_{1/2}$) of the Ti^{4+} (TiO$_2$) are observed at 458.83 ± 0.1 and 464.53 ± 0.1 for TNT, 458.3 ± 0.1 and 464.1 ± 0.1 for TNR, and 458.75 ± 0.1 and 464.5 ± 0.1 for the TGNP and TRGNF samples, respectively. A difference in binding energies of $\cong$5.7 eV between the Ti 2p$_{3/2}$ and Ti 2p$_{1/2}$ peaks of the doublet further confirmed the presence of TiO$_2$ on all sample surfaces.[11] Interestingly, the Ti 2p peak shifts to a lower binding energy in the TNR sample compared to the other samples, which can be attributed to the large concentration of oxygen vacancies created in the presence of NaOH during the hydrothermal process. These results suggest that the samples have different bonding environments.[35]

The calculated O/Ti ratios are shown in Table 2. As expected, pure TiO$_2$ (TNT) has a slight metal excess (or oxygen deficiency)

Table 1 XPS peak positions of fitted high-resolution spectra of C 1s, O 1s and Ti 2p for the TRGNF, TGNP, TNR and TNT samples

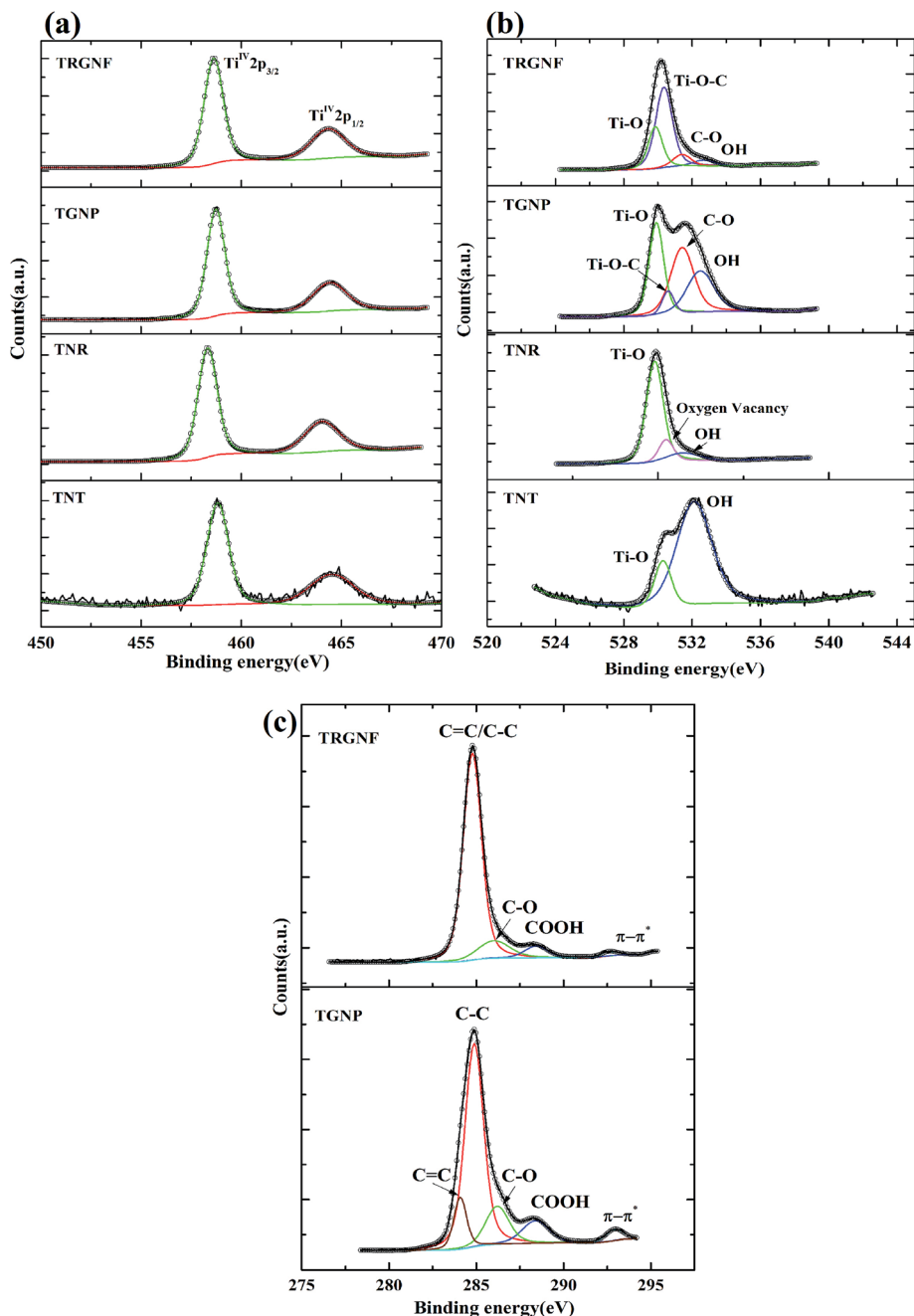| Sample	Binding energy (eV) for corresponding peak positions									
	Ti(IV) 2p$_{1/2}$	Ti(IV) 2p$_{3/2}$	C=C/C–C	C–O	–O–C=OH	π–π*	Ti–O	Ti–O–C	C–OH	O$_2{}^{2-}$	OH
NT	464.53	458.83	—	—	—	—	530.29	—	—	—	532.12
TNR	464.01	458.31	—	—	—	—	529.77	—	—	530.38	531.49
TGNP	464.41	458.73	284.08/284.88	286.2	288.39	292.93	529.91	530.60	531.42	—	532.48
TRGNF	464.32	458.62	284.78	286.04	288.39	292.62	529.89	530.39	531.46	—	532.72

Fig. 4 High-resolution XPS spectra: (a) Ti 2p (b) O 1s (c) and C 1s for TNT, TNR, TGNP, and TRGNF samples.

compared to the stoichiometric value, which is often observed in similar wide-bandgap n-type metal oxides.[36,37] The O/Ti ratio is gradually increased in TNR, TGNP and TRGNF, apparently because of their hydrothermal treatments with aqueous NaOH and GOs.

3.3.2. Analysis of O 1s spectrum. High-resolution XPS spectra of O 1s are presented in Fig. 4b. The spectra of all samples showed main peaks between 529.89 and 530.29 eV, which are related to oxygen in titanium dioxide (Ti–O–Ti).[38] The binding energy of 532.12 eV can be seen in Fig. 4b (TNT sample), which corresponds to hydroxyl groups (–OH) and physisorbed water.[39] The absence of annealing in the TNT film

resulted in a low-intensity of the Ti–O peak and high hydroxyl content, which can be attributed to defective sites on the TiO_2 film surfaces for absorption of H_2O molecules and to the rapid reaction of the mesoporous surface of TiO_2 with moisture to form hydroxyl.[40]

There is a peak with higher binding energy located at 530.38–530.6 eV, which originates from oxygen vacancies for TNR and Ti–O–C for the TGNP and TRGNF samples.[41,42] It should be noted that the oxygen vacancies and Ti–O–C bonding overlap in this range. As shown in Fig. 4b, the peak corresponding to the Ti–O–C bond increases in intensity when RGO is formed, which indicates a high degree of interaction between the organic and

inorganic components. The oxygen vacancy-related peak in TNR samples originates from the vigorous etching *via* NaOH, which removes some of the lattice and interstitial oxygen atoms from the crystal lattice. Although TRGNF samples are also etched by NaOH, any oxygen vacancy created by etching is compensated for by the presence of RGO within the hydrothermal environment.

A binding energy of 531.49 eV can also be seen in Fig. 4b (TNR sample) and is assigned to the hydroxyl groups. There are also two closely spaced peaks centered at 531.42 ± 0.04 and 532.48 ± 0.3 eV corresponding to C–OH and COOH bonds, respectively (the combined C–O peak in TGNP and TRGNF samples of Fig. 4b).[43] The difference in the intensity of these peaks between TGNP and TRGNF can be attributed to the loss of oxygen, which indicates a conversion of GO to RGO in the presence of NaOH during the hydrothermal process.

3.3.3. Analysis of C 1s spectrum. The C 1s spectrum of TGNP is split into five functional groups (Fig. 4c): a C=C bond at 284.08 eV, a C–C bond at 284.88 eV, a C–O bond at 286.2 eV, a O–C=O bond at 288.39 eV, and a π–π^* bond at 292.93 eV. Similarly, the high-resolution C 1s XPS spectrum of TRGNF is deconvoluted into four components around 284.78 eV, 286.04 eV, 288.39 eV, and 292.62 eV, respectively. The peak at 284.78 corresponds to the aliphatic C–C, whereas the other three peaks can be assigned to carbon atoms in different functional groups, such as hydroxyl or epoxy C–O, carboxylate carbon O–C=O bonds, and a π–π^* shake up satellite peak, respectively.[44,45] The resolution of the XPS spectrometer does not allow for peaks of C–C and C=C to be analyzed separately for the TRGNF film. Therefore, it will be treated as a single peak and compared with peaks corresponding to the carbon atoms bonded with other groups.

The CC/CO intensity ratio of TGNP is much lower (2.3) than that of TRGNF (14.2), where "CC" refers to the sum of C–C and C=C bonds and "CO" refers to all combinations of carbon and oxygen atom bonds, including C–O and C–C=O.[45] This is apparent because the areas of oxygen-containing functional group peaks decreased considerably in the TRGNF film due to the reduction process by alkaline NaOH solution and hydrothermal treatment. This indicates that an effective chemical reduction of the GO sheets occurred.[28] All these results indicate the incorporation of RGO into the titania matrix in the systems using the thermal-alkaline reduction and that alkaline reduction can reduce all kinds of oxygen-containing functional groups, indicating a higher current conductivity of TRGNF and efficiency of a particular reduction method.

3.4. Raman measurements

Raman spectroscopy is used to confirm the presence of GO/RGO and to monitor the chemical interaction between TiO_2 with GO and RGO in TGNP and TRGNF samples. The Raman spectra indicates some structural changes occurring during the chemical processing of GO to the reduced graphene oxide, as shown in Fig. 5. In TGNP sample the peaks are located at ~ 155, ~ 404, ~ 523 and ~ 643 cm^{-1} and for TRGNF at ~ 152,
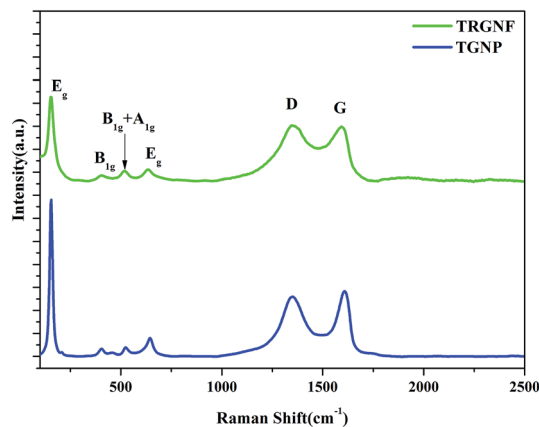

Fig. 5 Raman spectra of titania nanoparticle–GO composite (TGNP) and titania nanoflake–RGO composite (TRGNF).

~ 405, ~ 518 and ~ 635 cm^{-1} which correspond to the E_g, B_{1g}, $B_{1g} + A_{1g}$ and E_g modes of typical anatase phase of TiO_2 species.[25,36] Also, for both the samples there are two additional prominent peaks D (1349 cm^{-1}) and G (1609 cm^{-1}) for TGNP and D (1347 cm^{-1}) and G (1592 cm^{-1}) peaks for TRGNF, arising from the GO and RGO. Also, it's evident that after reduction of GO, the RGO in TRGNF sample is red-shifted from 1609 cm^{-1} to 1592 cm^{-1}. Similar red shift of the G peak is observed by How *et al.*[46] in their RGO/TiO_2 nanocomposites, which is attributed to the recovery of hexagonal network of C-atoms with defects *via* 'self-healing' effect.[47] The G-band is the Raman active E_{2g} mode of two-dimensional graphitic structures, which originates from the interplanar sp^2-bonded C–C stretching vibrations, whereas Raman D band originates from the vibrations of C atoms with dangling bonds in planer termination of disordered graphitic structures, which is the Raman active A_{1g} mode that corresponds to the structural disorders and mostly found at the edges.[48,49] The high I_D/I_G (I_D: intensity of the D band, I_G: intensity of the G band) ratio indicates numerous defect sites associated with the oxygen-containing functional groups in GO.[19] The TGNP shows a decreased I_D/I_G value ($I_D/I_G = 0.91$), as compared to the TRGNF ($I_D/I_G = 1.02$). This result is consistent with the literature, where similar increase in the I_D/I_G ratio is observed in TiO$_2$–RGO composites against GO structures.[50] This variation is manifested by two simultaneous reasons. Firstly, as described in Scheme 1, the reduction of GO leads to the (i) fragmentation of GO substructures, (ii) restoration of sp^2 bonds, and (iii) formation of new but smaller graphitic domains in RGO. Due to this reason, the average size of the sp^2 domains decreases, which leads to a decrease in the G peak intensity. Secondly, the smaller size of RGO leads to a large number of edges, which act as defects and contribute to the enhancement of the D peak. Hence, the overall I_D/I_G value increases in the TRGNF against TGNP samples. Therefore, this increased value of TRGNF shows reduction and restoration of the sp^2 of GO after the hydrothermal reduction process in presence of NaOH, which suggests successful reduction of GO and TRGNF is showing better graphitization.
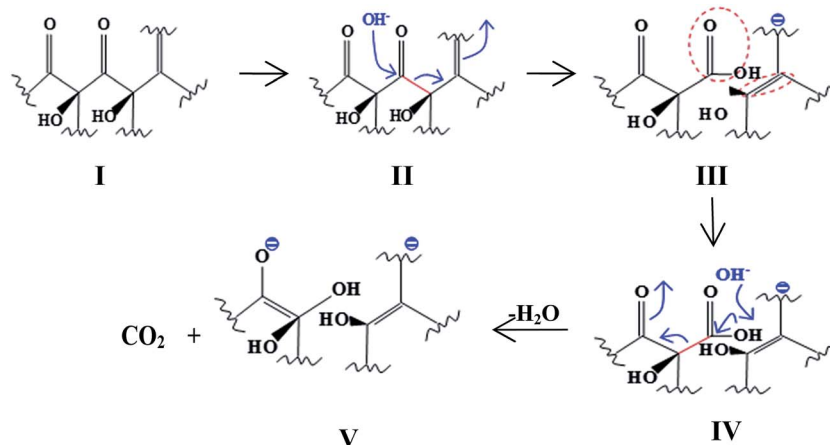
Scheme 1 The reduction schematics of a GO substructure under alkaline hydrothermal conditions.

3.5. Formation mechanism

One possible mechanism is the nucleation of Ti^{4+} on the TNT surface and formation of nanodroplets, as shown in Fig. 6(a) and (b). During the hydrothermal treatment, the solution containing titania nanotubes on Ti foil substrate was initially heated. The Ti^{4+} precursors can hydrolyze with water at the interface between water and the titania nanotube substrate, resulting in the formation of nanodroplets at all three reaction conditions. The specific conditions of the reaction environment (path (I) with NaOH/without GO, path (II) with NaOH and GO,

path (III) with GO/without NaOH) then determine the final nanostructure of the samples with increasing reaction time. For example, when only NaOH is present during the hydrothermal reaction (path I), NaOH acts as a vigorous etchant and the droplets grow with continuous hydrolysis. This is followed by the formation of a new interface between the hydrophilic TiO_2 and OH^- via dissolution and growth,[51,52] resulting in the formation of quasi-1D nanoribbons (TNR) (Fig. 6c). In the presence of NaOH and GO (path II), the etching process of TNT via NaOH is minimized because of the presence of GO, resulting in spreading and merging of the nanodroplets and leading to
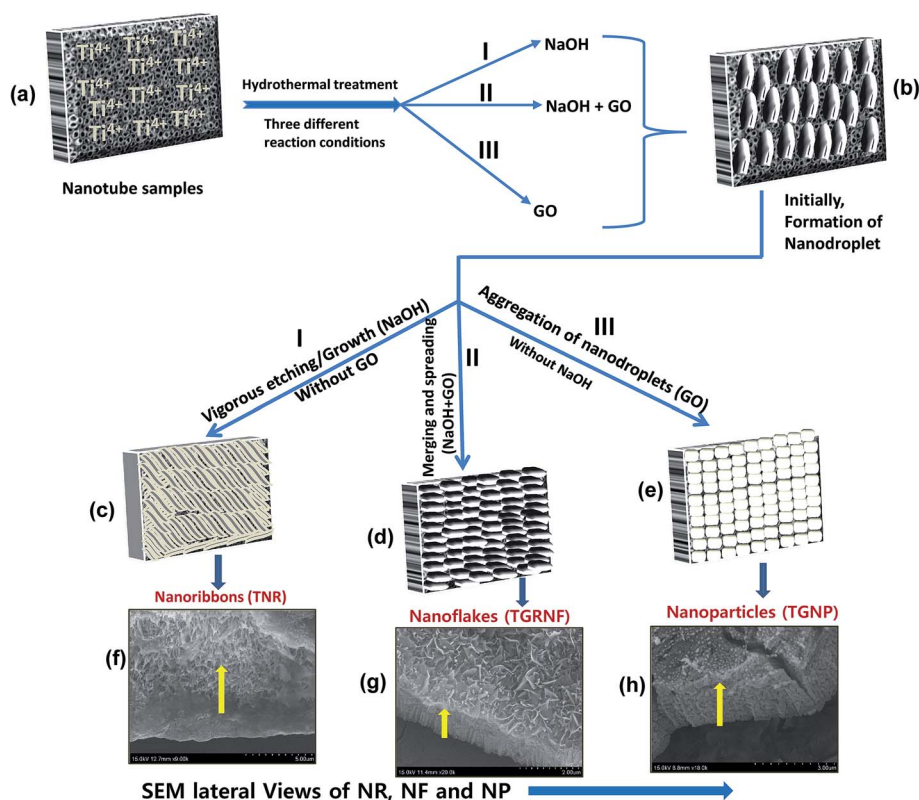

Fig. 6 Pictorial and schematic representation of the formation mechanism of TNR, TRGNF, and TGNP during the hydrothermal process.

the formation of quasi-2D titania nanoflakes. Additionally, NaOH acts as a reducing agent to convert GO to RGO to form the TRGNF hybrid (Fig. 6d).

Regarding the performance of NaOH as an etchant, under the applied hydrothermal conditions, TiO_2 reacts with NaOH solution to break the Ti–O–Ti bonds and the Na^+ ions are intercalated within the TiO_6 octahedral units to form $Na_2Ti_5O_{11}\cdot H_2O$ (sodium titanate):[53]

$$5TiO_2 + 2NaOH \rightarrow Na_2Ti_5O_{11}\cdot H_2O \quad (3)$$
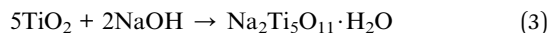
During post-hydrothermal treatment of the samples with 0.1 M HCl and washing (as explained in the Experimental section), $H_2Ti_5O_{11}\cdot H_2O$ (hydrated hydrogen pentatitanate) is formed by the ion exchange method (between Na^+ and H^+) as:[53]

$$Na_2Ti_5O_{11}\cdot H_2O + 2HCl \rightarrow H_2Ti_5O_{11}\cdot H_2O + 2NaCl \quad (4)$$
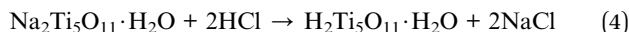
These by-products are then washed out with DI water to get etched surfaces.

As far as the performance of NaOH as reducing agent is concerned, it has been reported that under alkaline condition, GO can be reduced *via* deoxygenation (at room temperature with pH <10) or decarboxylation (at elevated temperature with pH >10) processes.[27,47] Under the current strong alkaline hydrothermal condition (2.5 M NaOH at 150 °C), decarboxylation is expected where –C–C– bond cleavage occurs in GO structure [I in Scheme 1] *via* nucleophilic attack of hydroxyl ions (of NaOH) on the carbonyl groups [II in Scheme 1] to form reduced structures containing carboxyl groups and –C=C– double bond structures [red circles in III of Scheme 1]. This structure is further decarboxylates *via* the similar –C–C– bond cleavage method [IV in Scheme 1], resulting in the formation of smaller substructures with more –C=C– double bonds [V in Scheme 1] and CO_2.[47]

Because of this –C=C– double bond formation, sp^2 is restored and RGO becomes more graphitized, as depicted by Raman measurements. Apparently, the results show less oxygen atom after the reduction of GO, as presented by the overall equation as follows:[47]

$$8C-OH \xrightarrow{150\,°C,\,pH>10} 3(-C=C-) + 2CO_2 + 4H_2O \quad (5)$$
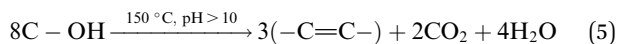
Wang *et al.*[54] synthesized RGO by the reduction of GO *via* removal of oxygen and repairing the aromatic structure using NaOH and the content of oxygen decreases with increasing the NaOH concentration.

In the presence of only GO (path III, *i.e.* no etching in the absence of NaOH), the aggregation of the nanodroplets leads to the formation of quasi-3D nanoparticles of titania and the simultaneous interaction of functional groups in the GO with titania, resulting in the formation of TGNP during the hydrothermal treatment[55] (Fig. 6e). Corresponding lateral views of the nanostructures are shown in Fig. 6f–h. It is clear that the nucleation, growth and oriented attachment are simultaneously involved in the overall hydrothermal process to obtain different nanostructures.

3.6. Electrochemical analysis

The advantages of the unique structures were investigated by testing the electrochemical performance of TNT, TNR, TGNP, and TRGNF. Fig. 7a shows the CV curves of the as-prepared electrode samples at a scan rate of 10 mV s⁻¹ in 1 M KCl electrolyte solution within an optimized potential range of −0.2 to +0.7 V. The CV plots typically show a quasi-rectangular shape, suggesting double layer capacitor behavior at the electrode–solution interface rather than faradaic reactions.[1] It is well known that the integrated area of the CV curve characterizes the ion adsorption capacity.[56] The CV curve of the TRGNF electrode has the largest area, followed by TGNP, TNR, and TNTs, confirming that the presence of RGO and GO help the electrosorption performance.

According to eqn (1), the estimated specific capacitance of the TRGNF and TGNP electrodes are 1.2 and 0.67 mF cm⁻², respectively, which are higher than those of TNT (0.24 mF cm⁻²) and TNR (0.13 mF cm⁻²) at 10 mV s⁻¹. Fig. 7b shows the specific capacitance *versus* scan rate for TRGNF, TGNP, TNR, and TNT electrodes. The specific capacitance decreases with increasing scan rate due to an ion exchange mechanism,[56] which is a common phenomenon. If the scan rate is low, the K^+ ions may have enough time to diffuse into the electrode, whereas at high scan rate, there is no time to diffuse into the sample. The lower degree diffusion of K^+ ions to the electrode decreases the specific capacitance value at higher scan rate.

The charge–discharge performance of all samples was investigated at different current densities within a potential window of −0.2 to 0.7 V *versus* the Ag/AgCl reference electrode using 1 M KCl as the electrolyte. Fig. 7c shows the characteristic potential curves *versus* cycle time for TNT, TNR, TGNP, and TRGNF electrodes at a current density of 1.0 μA cm⁻². The difference in curve profile with a slight bend in Fig. 7c could be caused by a distinct energy storage mechanism and faradaic pseudocapacitive reaction.[57]

Compared to the other two samples (TNT and TNR), the charge discharge curve of the TRGNF is substantially extended, followed by TGNP, as expected. This reveals excellent and improved capacitive behavior of these samples. The specific capacitances of the electrodes can be calculated based on the charge–discharge curves, and the results at various current densities are presented in Fig. 7d. The TNR, TNT, TGNP, and TRGNF samples showed successively increasing capacitances of 0.057, 0.170, 0.527, and 0.72 mF cm⁻², respectively, at a current density of 1.0 μA cm⁻² using eqn (2). As expected, TRGNF has better capacitance than the other samples, which is in agreement with the CV results.

At the high current density of 10 μA cm⁻², the TRGNF still showed a capacitance of 0.42 mF cm⁻², maintaining 51% of the capacitances and indicating that the TRGNF electrode would be more suitable for high-power applications. This improved specific capacitance of TRGNF and TGNP in comparison with TNR and TNT is due to the presence of graphene layers. In Fig. 7b and d, quasi-1D TNR shows the lowest capacitance values and it increases in the order of TNR < TNT < TGNP < TRGNF. It is well-known that active surface area is an important
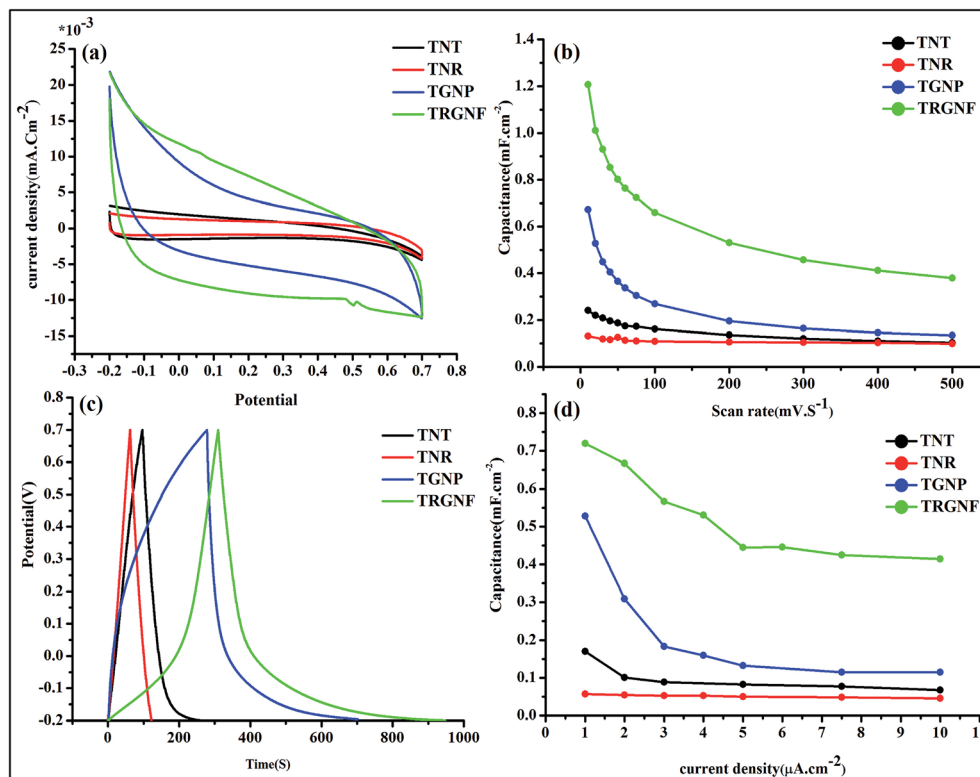
Fig. 7 (a) Cyclic voltammograms of TNT, TNR, TGNP, and TRGNF at 10 mV s^{-1}, (b) specific capacitance as a function of the scan rate obtained from the CV data, (c) galvanostatic charge−discharge curves at 1 μA cm^{-2}, (d) specific capacitance as a function of the current densities obtained from the charge−discharge data.

factor for the improved electrochemical performance of a material. For thin film based materials (as in the current case) the active surface area is directly related to the surface roughness[58] to provide a qualitative and reliable estimate of the effective surface area. Higher the surface roughness is, better is the active surface area to manifest improved electrochemical properties. Surface roughnesses of the TNT, TNR TGNP and TRGNF are analyzed using AFM. The AFM images are represented in Fig. S5.† The root mean square surface roughness (RMS) of the samples are obtained as 9 ± 1, 11 ± 1, 12 ± 1, 14 ± 1 nm for TNR, TNT, TGNP and TRGNF samples, respectively. The least RMS roughness obtained for TNR sample and its increasing order of TNR < TNT < TGNP < TRGNF indicates that the active surface area also increases in the same order, which further increases the capacitance per unit area of the electrodes accordingly, and thus well-correlated with the capacitance data.

Also, the unique morphology, structure, and interconnectivity of the active materials enhance the charge storage and ion exchange,[59] which further improves the capacitance by increasing the effective surface area. The better capacitive performance of TRGNF over TGNP is due to its unique nanostructure. The individual nanoflakes considerably improve the electrode/electrolyte contact area, reduce the ion diffusion paths, speed up the ionic exchange, and greatly increase the number of electroactive sites.[60] The effect of the number of dimension on the electrochemical performance is also analyzed. The quasi-1D TNR and TNT showed lowest

capacitance and it is improved in 3D TGNP and 2D TRGNF samples. This variation is mainly due to some physical and physicochemical properties. 1D TNR and TNT showed least capacitance values mainly because of least surface roughness (in TNR: ~9 nm, TNT: ~11 nm), and hence, least active surface area. Therefore in 1D TNR and TNT samples, the capacitance variation is mainly due to the physical reason. The 3D TGNP samples showed better capacitance than 1D structures because of higher surface roughness (~12 nm) as well as the presence of GO, which is reported to have good electrochemical properties.[61] The 2D TRGNF sample showed best capacitance mainly because of having highest surface roughness (~14 nm), so also highest active surface area, along with the presence of RGO, which is having good electrochemical properties.[62] Therefore, the superior electrochemical performance of TGNP and TRGNF samples are due to the physicochemical reason. Although the general notion is that 1D nanomaterials have higher surface-to-volume ratio than 2D and 3D nanomaterials[63] but the correlation is not that straight forward and depends on the particular surface nanostructure,[64] and especially for interfacial applications of thin film based nanomaterials (as in the current case), surface roughness is one of the important and relevant parameters for the estimation of active surface sites. Since 1D TNR and TNT samples showed least RMS surface roughness, corresponding electrochemical properties are also inferior to the 2D TRGNF and 3D TGNP samples.

Fig. 8a and b show comparative Nyquist plots of the TNT, TNR, TGNP, and TRGNF electrodes determined by EIS in the frequency range 50 kHz to 0.001 kHz at open circuit potentials in the KCl electrolyte. The EIS spectra of a supercapacitor electrode are usually deconvoluted into two segments: a small semicircle in the high frequency region and a straight line in the low frequency regions. The arc for the range of very high frequency is generated at the electrode/electrolyte interface and is called the equivalent series resistance (ESR). The linear portion at the low frequencies is the Warburg resistance and is due to the frequency dependence of ion diffusion and transport from the electrolyte to the electrode surfaces.[65] As shown in Fig. 8a, the semi-circle in the high frequency region in the Nyquist plots of all samples is not very significant. This probably occurs because of the very small charge-transfer resistance and suggests negligible interfacial polarization resistance. Furthermore, the charge transfer of the TRGNF and TGNP with nanoflakes and nanoparticles can be improved by the enhanced contact area between the salt solution and the electrode.

The intersection of the curves at the real axis (x-axis) in the range of high frequency represents the equivalent series resistance (ESR), which is about 2.18, 2.53, 3.89, and 5.7 Ω for the TRGNF, TGNP, TNT, and TNR samples, respectively (Fig. 8b). TRGNF has a lower resistance, which is important because less power and energy will be wasted as unwanted heat during the charge–discharge processes.[2] This lower ESR indicates good electronic conductivity and indicates suitability for supercapacitor applications due to the presence of reduced graphene.[55] RGO–TiO₂ nanoflakes on the TNT surface decrease the

inner resistance of TRGNF, which is in good agreement with the high diffusion coefficient observed in the CV and charge–discharge curves. Also, the smaller ESR means that the TRGNF electrode will have less internal loss and greater charge transport.[56] It is apparent that the TRGNF electrode has the lowest series resistance (ESR) and the most ideal straight line, indicating a faster electrolyte diffusion, and better electrical conductivity and capacitive behavior than TNT, TNR and TGNP electrodes. The faster electrolyte diffusion in TRGNF can be ascribed to higher surface area (from AFM data) and it gives better contact with the electrolyte. In addition, TRGNF has higher degree of graphitization than TGNP according to XPS and Raman analysis, thus a higher conductivity is obtained. The surface properties of electrode materials such as surface roughness and surface area are crucial to the electrochemical performance. Electrical double layer capacitors (EDLCs) that are based on electrostatic charge diffusion and accumulation at the electrode/electrolyte interface. As stated earlier roughening the surface will increase the surface which further increases the capacitance per unit electrode area. The capacitance is directly proportional to the surface area and inversely proportional to the charge separation. The capacitance behavior is influenced by interplay between the characteristic roughness and Debye length which associated with the surface–electrolyte interface.[66] Debye length refers to the shortest distance over which an effective separation of charges occurs. In this study, capacitance increases linearly with the RMS roughness of the surface, indicating that the capacitance is indeed a function of the microscopic surface area. Therefore, the electrochemical
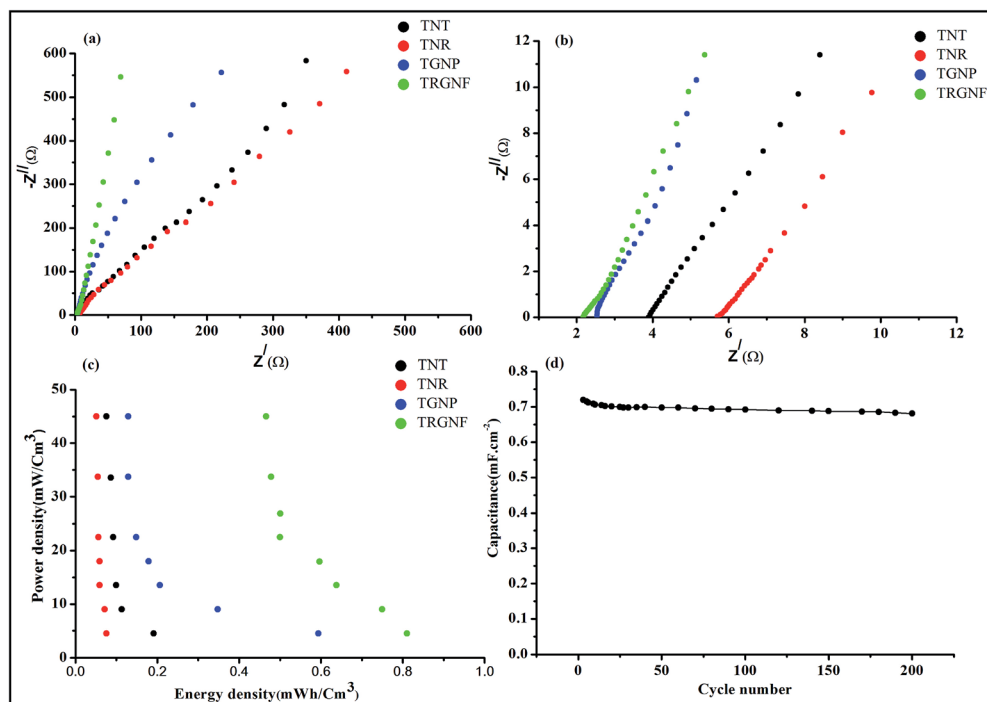

Fig. 8 (a) Nyquist plots of the electrochemical impedance spectra for all synthesized samples, (b) impedance of samples in the high frequency region, (c) Ragone plots of power density *versus* energy density calculated from galvanostatic discharge for all the samples, (d) cycle life of TRGNF at 1 µA cm⁻² over 200 cycles.

double layer will follow the surface closely and parallel to it at every point, so the effect on the capacitance will be due only to an overall increase in surface area. Therefore, the combination of both highly accessible surface area and higher conductivity due to formation of individual nano flakes and RGO in TRGNF electrode will be the contributing factors for the enhanced electrochemical performance obtained here, even though the capacitance of bare GO is obtained higher than RGO (as shown and explained in Fig. S6†).

The power density and energy density were calculated from the galvanostatic discharge curves and are plotted in a Ragone diagram (Fig. 8c), which is used to determine the electrochemical performance. These densities can be estimated using the following equations:[4]

$$E = 0.5CV \tag{6}$$

$$P = E/t \tag{7}$$

where P, C, V, t, and E represent the power density (W cm^{-3}), specific capacitance based on the volume of the electroactive material (F cm^{-3}), cell voltage for charging and discharging (V), discharge time (s), and energy density (W h cm^{-3}), respectively. As shown in the plots, the supercapacitor with TRGNF shows greatly superior electrochemical properties with enhanced power density and energy density compared with those based on TNT and GO (i.e., TNT, TNR, and TGNP). It is clear that the device shows a maximum energy density of 0.81 mW h cm^{-3} with a power density of 45 mW cm^{-3} at an energy density of 0.47 mW h cm^{-3}. These results indicate that the TRGNF can provide high energy density without much loss of power density. The results are higher than for similar materials, including TNT (0.19 mW h cm^{-3}), TNR (0.075 mW h cm^{-3}), and TGNP (0.59 mW h cm^{-3}) at a power density of 4.5 mW cm^{-3}. The superior performance is mainly due to the high capacitance of TRGNF and excellent rate capability.

The cyclic stability was examined for the TRGNF electrode from six time repetitions of charge–discharge experiments at a constant current density of 1 μA cm^{-2} for 200 cycles each (using the same sample electrode). The results from the sixth experiment are presented in Fig. 8d. There was a small decrease (∼6%) in the specific capacitance during the first 30 cycles, and then it remained almost constant for the rest of the cycles (∼94 retention). This indicates excellent stability and lifetime of the TRGNF electrode, which can be used as a sustainable energy storage device for supercapacitor applications. The superior capacitance retention of the TRGNF electrodes can be attributed to the lesser surface-structural degradation during repeated charge/discharge processes.

4. Conclusions

TNTs were fabricated on Ti substrate by electrochemical anodization, and then TNR, TRGNF, and TGNP were synthesized by a hydrothermal process using the TNTs, NaOH, and GO. The electrochemical specific capacitance of the TNR, TGNP, and TRGNF was studied and compared with that of TNTs. The

TRGNF electrode exhibits a maximum specific capacitance of 1.2 mF cm^{-2} at a scan rate of 10 mV s^{-1} in an electrolyte solution of 1 M KCl. The unique morphology and structure of the TRGNF result in good rate performance (51% retention of the initial capacitance from 1 to 10 μA cm^{-2}). The improved electrochemical performance of the TRGNF structure make it suitable as a prospective electrode material for electrochemical energy storage applications. The TRGNF sample showed a maximum energy density of 0.81 mW h cm^{-3} at 4.5 mW cm^{-3} and power density of 45 mW cm^{-3} at an energy density of 0.47 mW h cm^{-3}. The results indicate that the TRGNF can provide high energy density without much loss of power density.

References

1 C. Zhou and J. Liu, *Nanotechnology*, 2014, **25**, 035402.
2 S. Wang and R. A. W. Dryfe, *J. Mater. Chem. A*, 2013, **1**, 5279–5283.
3 B. G. Choi, J. Hong, W. H. Hong, P. T. Hammond and H. Park, *ACS Nano*, 2011, **5**, 7205–7213.
4 X. Lu, G. Wang, T. Zhai, M. Yu, J. Gan, Y. Tong and Y. Li, *Nano Lett.*, 2012, **12**, 1690–1696.
5 T. Kuila, A. K. Mishra, P. Khanra, N. H. Kim and J. H. Lee, *Nanoscale*, 2013, **5**, 52–71.
6 A. N. Banerjee, *Nanotechnol., Sci. Appl.*, 2011, **4**, 35–65.
7 R. Daghrir, P. Drogui and D. Robert, *Ind. Eng. Chem. Res.*, 2013, **52**, 3581–3599.
8 H. H. Ou and S. L. Lo, *Sep. Purif. Technol.*, 2007, **58**, 179–191.
9 F. Fabregat-Santiago, H. Randriamahazaka, A. Zaban, J. Garcia-Cañadas, G. Garcia-Belmonte and J. Bisquert, *Phys. Chem. Chem. Phys.*, 2006, **8**, 1827–1833.
10 X. Sun, M. Xie, G. Wang, H. Sun, A. S. Cavanagh, J. J. Travis, S. M. George and J. Lian, *J. Electrochem. Soc.*, 2012, **159**, A364.
11 M. Salari, S. H. Aboutalebi, K. Konstantinov and H. K. Liu, *Phys. Chem. Chem. Phys.*, 2011, **13**, 5038–5041.
12 B. Y. S. Chang, N. M. Huang, M. N. An'amt, A. R. Marlinda, Y. Norazriena, M. R. Muhamad, I. Harrison, H. N. Lim and C. H. Chia, *Int. J. Nanomed.*, 2012, **7**, 3379–3387.
13 N. Li, G. Liu, C. Zhen, F. Li, L. Zhang and H. M. Cheng, *Adv. Funct. Mater.*, 2011, **21**, 1717–1722.
14 H. J. Choi, S. M. Jung, J. M. Seo, D. W. Chang, L. Dai and J. B. Baek, *Nano Energy*, 2012, **1**, 534–551.
15 S. Mao and J. Chen, *Nanoscale*, 2015, 6924–6943.
16 K. S. Novoselov, *Phys. World*, 2009, 27–30.
17 D. R. Dreyer, S. Park, C. W. Bielawski and R. S. Ruoff, *Chem. Soc. Rev.*, 2010, **39**, 228–240.
18 M. Zhen, S. Guo, G. Gao, Z. Zhou and L. Liu, *Chem. Commun.*, 2015, **51**, 507–510.
19 C. Xiang, M. Li, M. Zhi, A. Manivannan and N. Wu, *J. Mater. Chem.*, 2012, **22**, 19161.

20 J. Kim, W.-H. Khoh, B.-H. Wee and J.-D. Hong, *RSC Adv.*, 2015, **5**, 9904–9911.

21 V. C. Anitha, D. Menon, S. V. Nair and R. Prasanth, *Electrochim. Acta*, 2010, **55**, 3703–3713.

22 V. C. Anitha, A. N. Banerjee, S. W. Joo and B. K. Min, *J. Ind. Eng. Chem.*, 2015, **29**, 227–237.

23 V. C. Anitha, J.-H. Lee, J. Lee, A. Narayan Banerjee, S. Woo Joo and B. Ki Min, *Nanotechnology*, 2015, **26**, 065102.

24 N. M. Huang, H. N. Lim, C. H. Chia, M. a. Yarmo and M. R. Muhamad, *Int. J. Nanomed.*, 2011, **6**, 3443–3448.

25 C. Zhai, M. Zhu, Y. Lu, F. Ren, C. Wang, Y. Du and P. Yang, *Phys. Chem. Chem. Phys.*, 2014, **16**, 14800–14807.

26 S.-T. Han, Y. Zhou, C. Wang, L. He, W. Zhang and V. A. L. Roy, *Adv. Mater.*, 2013, **25**, 872–877.

27 A. Valipour, N. Hamnabard and Y.-H. Ahn, *RSC Adv.*, 2015, **5**, 92970–92979.

28 C. Chen, W. Kong, H.-M. Duan and J. Zhang, *Phys. Chem. Chem. Phys.*, 2014, **20**, 12858–12864.

29 S. H. Huh, *Physics and Applications of Graphene-Experiments*, ed. Milkhailov, 2011, pp. 73–90.

30 M. L. Vera, M. A. Alterach, M. R. Rosenberger, D. G. Lamas, C. E. Schvezov and A. E. Ares, *LNLS Activity Report*, 2009, pp. 1–2.

31 R. M. Zaid, F. Chin, E. Yi, L. Teo, E. Ng and K. Feng, *Arabian J. Chem.*, 2014, **8**, 560–569.

32 J.-H. Yun, R. J. Wong, Y. H. Ng, A. Du and R. Amal, *RSC Adv.*, 2012, **2**, 8164.

33 D. B. Haddow, S. R. Hadfield, M. Street and C. Crescent, *J. Mater. Sci.: Mater. Med.*, 1996, **7**, 255–260.

34 M. Oku, K. Wagatsuma and S. Kohiki, *Phys. Chem. Chem. Phys.*, 1999, **1**, 5327–5331.

35 B. Santara, P. K. Giri, S. Dhara, K. Imakita and M. Fujii, *J. Phys. D: Appl. Phys.*, 2014, **47**, 235304.

36 V. C. Anitha, A. N. Banerjee and S. W. Joo, *J. Mater. Sci.*, 2015, **50**, 7495–7536.

37 A. N. Banerjee, S. W. Joo and B.-K. Min, *J. Nanosci. Nanotechnol.*, 2014, **14**, 7970–7975.

38 X. Ma, X. Suo, H. Cao, J. Guo, L. Lv, H. Sun and M. Zheng, *Phys. Chem. Chem. Phys.*, 2014, **16**, 12731.

39 M. S. Kim, T.-W. Lee and J. H. Park, *J. Electrochem. Soc.*, 2009, **156**, A584.

40 S. Agarwala and G. W. Ho, *Mater. Lett.*, 2009, **63**, 1624–1627.

41 T. Lu, R. Zhang, C. Hu, F. Chen, S. Duo and Q. Hu, *Phys. Chem. Chem. Phys.*, 2013, **15**, 12963–12970.

42 S. Y. Park, S. Kim, J. Yoo, K.-H. Lim, E. Lee, K. Kim, J. Kim and Y. S. Kim, *RSC Adv.*, 2014, 11295–11299.

43 H. Zhang, S. Shuang, G. Wang, Y. Guo, X. Tong, P. Yang, A. Chen, C. Dong and Y. Qin, *RSC Adv.*, 2015, **5**, 4343–4349.

44 Y. Li, H. Chen, L. Y. Voo, J. Ji, G. Zhang, G. Zhang, F. Zhang and X. Fan, *J. Mater. Chem.*, 2012, **22**, 15021.

45 H. Zhang, P. Xu, G. Du, Z. Chen, K. Oh, D. Pan and Z. Jiao, *Nano Res.*, 2011, **4**, 274–283.

46 G. T. S. How, A. Pandikumar, H. N. Ming and L. H. Ngee, *Sci. Rep.*, 2014, **4**, 2–9.

47 Q. Zheng, B. Zhang, X. Lin, X. Shen, N. Yousefi, Z.-D. Huang, Z. Li and J.-K. Kim, *J. Mater. Chem.*, 2012, 25072–25082.

48 A. N. Banerjee, B.-K. Min and S. W. Joo, *Appl. Surf. Sci.*, 2013, **268**, 588–600.

49 A. N. Banerjee, S. W. Joo and B. K. Min, *Thin Solid Films*, 2013, **537**, 49–57.

50 J. Shen, B. Yan, M. Shi, H. Ma, N. Li and M. Ye, *J. Mater. Chem.*, 2011, **21**, 3415.

51 V. C. Anitha, A. N. Banerjee, S. W. Joo and B. K. Min, *Nanotechnology*, 2015, **26**, 355705.

52 V. V. Divya Rani, K. Manzoor, D. Menon, N. Selvamurugan and S. V. Nair, *Nanotechnology*, 2009, **20**, 195101.

53 B. Santara and P. K. Giri, *Mater. Chem. Phys.*, 2013, **137**, 928–936.

54 W. Huan, T. Hong-wei, W. Xin-wei, Q. Liang, W. Shu-min, W. Xing-li, Z. Wei-tao and L. Yi-chun, *Chem. Res. Chin. Univ.*, 2011, **27**, 857–861.

55 B. Liu, A. Khare and E. S. Aydil, *Chem. Commun.*, 2012, **48**, 8565.

56 H. Wang, L. Shi, T. Yan, J. Zhang, Q. Zhong and D. Zhang, *J. Mater. Chem. A*, 2014, **2**, 4739–4750.

57 P. Wen, P. Gong, J. Sun, J. Wang and S. Yang, *J. Mater. Chem. A*, 2015, **3**, 13874–13883.

58 M. Katsikogianni and Y. F. Missirlis, *Eur. Cells Mater.*, 2004, **8**, 37–57.

59 S. H. Aboutalebi, A. T. Chidembo, M. Salari, K. Konstantinov, D. Wexler, H. K. Liu and S. X. Dou, *Energy Environ. Sci.*, 2011, **4**, 1855.

60 X. Yan, X. Tong, J. Wang, C. Gong, M. Zhang and L. Liang, *Mater. Lett.*, 2013, **106**, 250–253.

61 Y. Matsumoto, H. Tateishi, M. Koinuma, Y. Kamei, C. Ogata, K. Gezuhara, K. Hatakeyama, S. Hayami, T. Taniguchi and A. Funatsu, *J. Electroanal. Chem.*, 2013, **704**, 233–241.

62 K. Satheesh and R. Jayavel, *Mater. Lett.*, 2013, **113**, 5–8.

63 X. C. Changhong ke, *Anisotropic Nanomaterials: Preparation, Properties, and Applications*, ed. Q. Li, Springer, NY, 2015, ch. 10.

64 M. R. Alenezi, S. J. Henley, N. G. Emerson and S. R. P. Silva, *Nanoscale*, 2014, **6**, 235–247.

65 G. Lui, J.-Y. Liao, A. Duan, Z. Zhang, M. Fowler and A. Yu, *J. Mater. Chem. A*, 2013, **1**, 12255–12262.

66 G. M. Thomas, thesis, WPI, 2012.